This is the Pre-Published Version.

This document is the Accepted Manuscript version of a Published Work that appeared in final form in Nano Letters, copyright © 2023 American Chemical Society after peer review and technical editing by the publisher. To access the final edited and published work see https://doi.org/10.1021/acs.nanolett.3c02882.

Hollow-carbon confinement annealing: a new synthetic approach to make high-entropy solid-solution and intermetallic nanoparticles

Yezhou Hu[a §], Zhihang Xu[a §], Xuyun Guo[a], Pei Xiong[a], Chao Xu[a], Changsheng Chen[a], Qian Zhang[b], Shuang Wang[b], Tai-Sing Wu[c], Yun-Liang Soo[d], Molly Meng-Jung Li[a], Deli Wang[b], Ye Zhu*[a]

[a] Department of Applied Physics, Research Institute for Smart Energy, The Hong Kong Polytechnic University, Hung Hom, Hong Kong, China

[b]Key Laboratory of Material Chemistry for Energy Conversion and Storage (Huazhong University of Science and Technology), Ministry of Education, Hubei Key Laboratory of Material Chemistry and Service Failure, School of Chemistry and Chemical Engineering, Huazhong University of Science and Technology, Wuhan 430074, P. R. China

[c] National Synchrotron Radiation Research Center, Hsinchu, 30076, Taiwan

[d] Department of Physics, National Tsing Hua University, Hsinchu, 30013, Taiwan

[§] These authors contributed equally to this work.

* Corresponding author

E-mail: yezhu@polyu.edu.hk (Ye Zhu)

ABSTRACT: High-entropy alloy (HEA) nanoparticles (NPs) have been emerging with superior compositional tunability and multi-elemental synergy, presenting a unique platform for material discovery and performance optimization. Here we report a synthetic approach utilizing hollow-carbon confinement in the ordinary furnace annealing to achieve the non-equilibrium HEA-NPs such as $Pt_{0.45}Fe_{0.18}Co_{0.12}Ni_{0.15}Mn_{0.10}$ with uniform size ~5.9 nm. The facile temperature control allows us not only to reveal the detailed reaction pathway through *ex situ* characterization, but also to tailor the HEA-NP structure from the crystalline solid solution to intermetallic. The pre-confinement of metal precursors is the key to ensure the uniform distribution of metal nanoparticles with confined volume, which is essential to prevent the thermodynamically favored phase separation even during the ordinary furnace annealing. Besides, the synthesized HEA-NPs exhibits remarkable activity and stability in oxygen reduction catalysis. The demonstrated synthetic approach may significantly expand the scope of HEA-NPs with uncharted composition and performance.

KEYWORDS: high-entropy alloy, high-entropy solid-solution, hollow-carbon confinement, Pt-based intermetallics, oxygen reduction reaction

High entropy alloys (HEAs), typically containing multiple elements randomly intermixed to possess high configuration entropy, represent one of the most complex materials with extraordinary functionalities exceeding conventional alloys[1-4]. With the reduced dimension to nanoscale, HEA nanoparticles (HEA-NPs) have drawn significant attention for their widely tunable compositions and properties, promising for various catalysis, energy[3, 5-7], environmental[8] and biomedical applications[9]. For example, the enormous diversity in the adsorption sites of HEA-NP surfaces gives rise to broadened and nearly continuous adsorption energy levels, which is particularly beneficial for multistep reactions involving adsorption of various intermediates[10, 11]. Combining with their enhanced structural stability, HEA-NPs have been used as high-performance catalysts for energy- and environment-relevant reactions including oxygen reduction reaction (ORR)[5], ammonia oxidation[12] and decomposition[13]. Manufacturing HEA-NPs, however, remains a grand challenge owing to the fundamental conflict between high-temperature synthesis required for multi-element intermixing and NP aggregation at high temperature.[12-20] HEA-NPs are initially obtained by thermal-shock-based methods[12-15], which requires rapid quench with carefully chosen rates to control kinetics just right for the non-equilibrium HEA: Too rapid cooling can cause structure amorphization with degraded crystallinity, while too slow cooling leads to thermodynamic-driven phase separation and nanoparticle aggregation[12]. The ordinary furnace annealing has been considered to be too slow to avoid phase separation, and thus incapable of achieving single-phase HEA-NPs. Even though thermal conversion of core@shell NPs to HEA-NPs has been recently demonstrated with slow annealing, so far it can only make fully intermixed solid-solution NPs but is incapable of achieving intermetallic HEA NPs.[19,20] Solution-based methods such as solvothermal synthesis and low-temperature co-reduction have also been established,[16-18] but are normally limited to metals with low melting points and high reduction potentials (Bi, Sn and Rh et al.). Their application on high-melting-point metals may be inhibited by their slow atomic diffusion at low temperature.

In this work, we demonstrate a novel approach utilizing volume confinement to stabilize the non-equilibrium HEA-NPs, enabling their synthesis even using the ordinary furnace annealing without any special control over kinetics. As a proof of concept, we have synthesized $Pt_{0.45}Fe_{0.18}Co_{0.12}Ni_{0.15}Mn_{0.10}$ HEA-NPs with uniform size ~5.9 nm using carbon-confinement furnace annealing. Through tuning the annealing temperature, HEA-NPs with the structure of both crystalline solid solution and intermetallic can be achieved in the single phase without elemental segregation or phase separation. The resultant hollow-carbon support further ensures sufficient exposed surface, enabling exceptional activity and stability of the synthesized HEA-NPs in ORR catalysis. The critical role of volume confinement on HEA-NP formation will also be discussed, which represents a promising strategy to further expand the scope of achievable HEA-NPs.

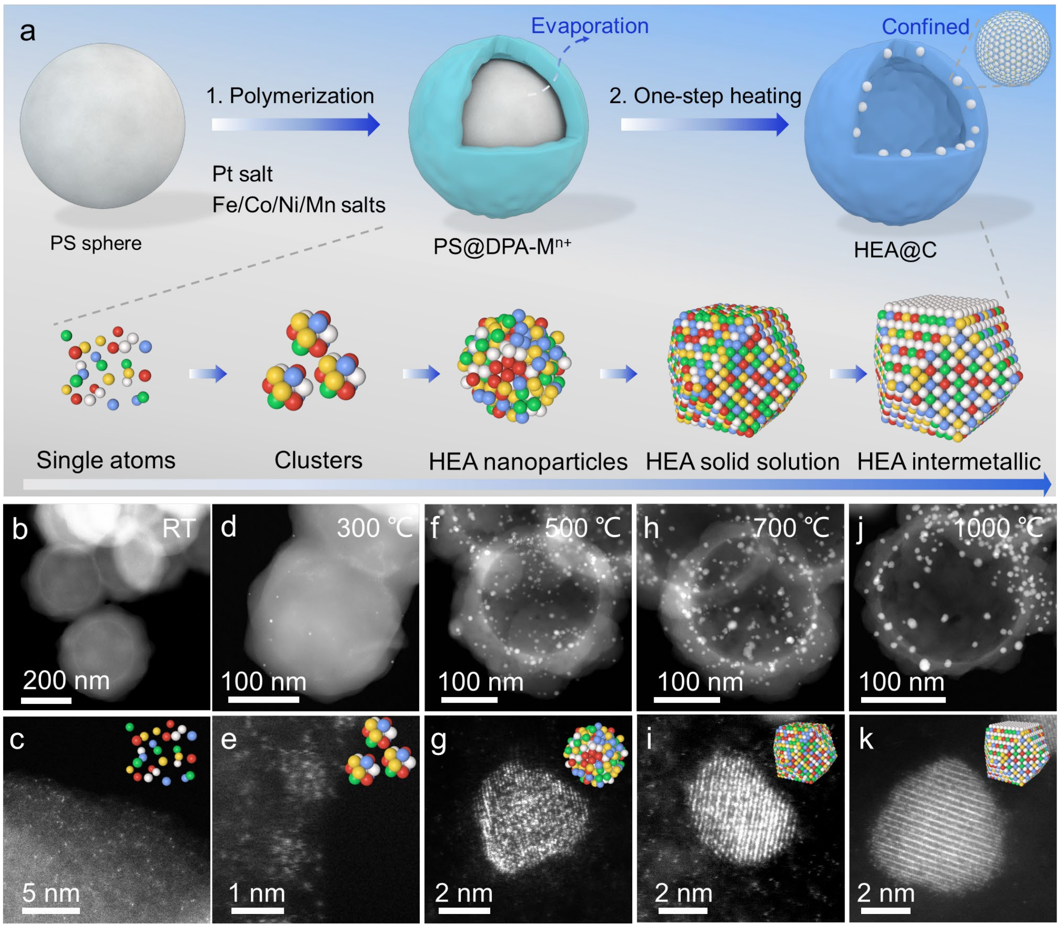

Figure 1. (a) Schematic diagram of the hollow-carbon confinement furnace annealing to form HEA-NPs with various structures. (b-k) STEM images of precursors treated at different temperatures, with the structure models shown in the insets.

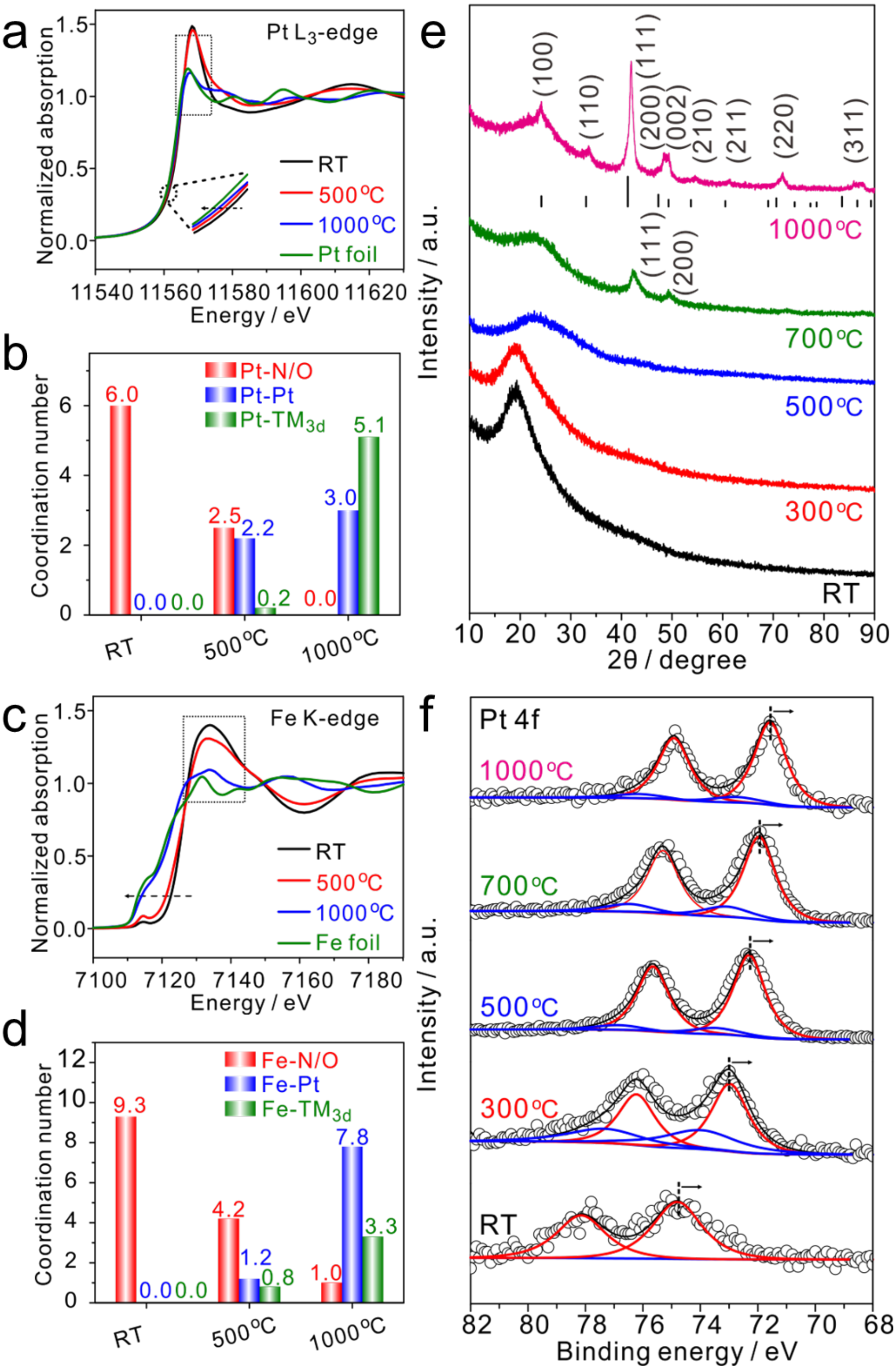

Figure 2. (a) Pt L_3-edge XANES spectra of precursors treated at different temperatures, and (b) corresponding fitting results of coordination numbers. (c) Fe K-edge XANES spectra of precursors treated at different temperatures, and (d) corresponding fitting

results of coordination numbers. (e) XRD patterns (standard PtFe intermetallic (PDF card #03-065-1051) is used as reference) and (f) Pt 4f XPS spectra of precursors treated at different temperatures.

The process of hollow-carbon confinement furnace annealing is illustrated in **Figure 1a** using $Pt_{0.45}Fe_{0.18}Co_{0.12}Ni_{0.15}Mn_{0.10}$ HEA-NPs as an example. First, the metal precursors (H_2PtCl_6, $FeCl_2$, $CoCl_2$, $NiCl_2$ and $MnCl_2$) are mixed in the tris-HCl buffering solution, with polystyrene (PS) nanospheres added. After fully intermixing, the dopamine polymer is then introduced and polymerized to form polydopamine layers via oxidative polymerization. Benefiting from the abundant functional groups (catechol, amine and imine), polydopamine can easily functionalize various substrates (even the low energy surface, e.g. PS). These functional groups provide rich anchoring sites to chelate with the metal ions, which effectively confine metal atoms on the surface of PS spheres (denoted as PS@DPA-M^{n+})[21]. The core-shell structure is confirmed by the electron energy-loss spectroscopy (EELS) on scanning transmission electron microscopy (STEM) shown in **Figure S1**. Besides, the formed polydopamine-M^{n+} layer is revealed by the STEM imaging (**Figure 1b-c**) and energy dispersive spectroscopy (EDS) mapping (**Figure S2a-f**).

The PS@DPA-M^{n+} precursors can be collected after centrifugation and drying, in which the metal elements are in the form of single atoms, as revealed by STEM imaging (**Figure 1b-c**). X-ray absorption near edge structure (XANES) of X-ray absorption spectroscopy (XAS) unveils high oxidation states for metals (**Figure 2a and c**). Together with the negative shifts of N 1s and O 1s binding energies detected by X-ray photoemission spectroscopy (XPS, **Figure S3a-b**), it indicates that the single metal atoms are anchored on the hydroxy and amino groups of dopamine as illustrated in **Figure S3c**. This is verified explicitly by the extended X-ray absorption fine structure (EXAFS) analysis, which reveals dominant metal-N/O bonding in PS@DPA-M^{n+} (**Figure S4**). X-ray diffraction (XRD) only detects a broad peak corresponding to the amorphous phase in PS nanospheres and polydopamine (**Figure 2e**), consistent with the single-atom state of metal elements. EDS mapping further shows the uniform distribution of all metal elements (**Figure S2a-f**), which is ideal for the subsequent heat treatment.

By heating PS@DPA-M^{n+} based on furnace annealing in N_2/H_2 atmosphere, the polydopamine layer can be carbonized to form carbon shells, while the metal atoms are released gradually to form the carbon-confined nanoparticles. The slow heating rate (~5 °C/min) of furnace annealing allows us to suspend at intermediate temperatures and to pinpoint the reaction products using TEM/STEM, XRD, XPS, and XAS in the *ex situ* manner. As shown in **Figure 1d-e**, **Figure S5 and Figure S6a,** heating at 300 °C gives rise to many high entropy nanoclusters formed by the released metal atoms, coexisting with the remaining anchored single metal atoms. Such nanoclusters cannot be detected by XRD (**Figure 2e**). XPS identifies the Pt valence to be +2 and +4 (**Figure 2f** and **Figure S6b-c**), indicating that most Pt atoms are still bonded to N/O atoms in polydopamine and the valence reduction at this low temperature is still limited.

When heating samples to 500 °C, PS nanospheres decompose and create the hollow structure with the carbon shells only (**Figure 1f**). Meanwhile, plenty of metal atoms are released for nanoclusters to grow into nanoparticles ~4.6 nm in size (**Figure 1g and Figure S7**). XANES detects the reduction of Pt and Fe based on their lower white-line intensity compared to PS@DPA-M^{n+} at room temperature (**Figure 2a and 2c**). EXAFS further reveals a decrease of Pt-N/O and Fe-N/O bonds accompanied by an increase of Pt-Pt and Pt-3d Transition metal (TM$_{3d}$) bonds (**Figure 2b and 2d**, with relevant fitting parameters shown in **Table S1-2**). XRD is still insensitive to detect such nanoparticles (**Figure 2e**), possibly owing to their ultrasmall size as well as low crystallinity and high defect density.

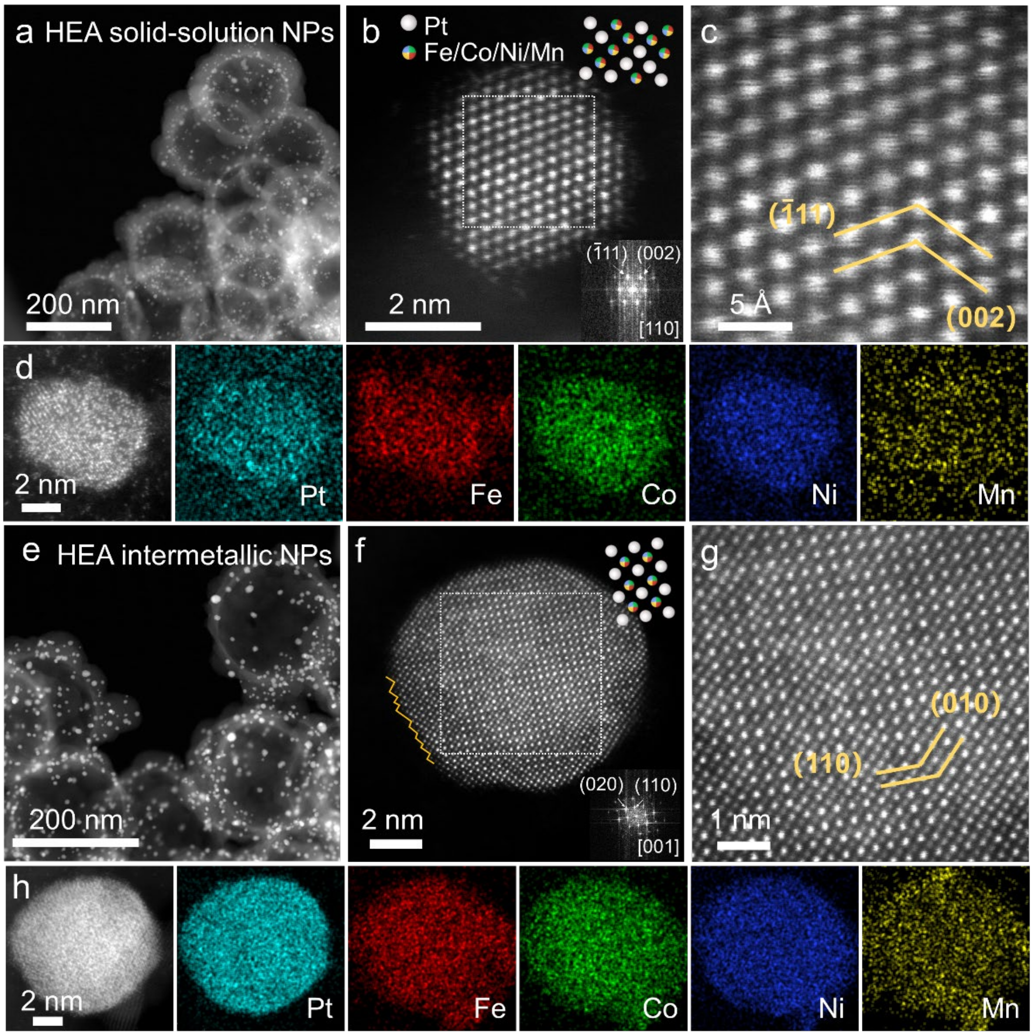

Figure 3. (a-c) HAADF-STEM images and (d) EDS elemental maps of HEA solid-solution NPs. (e-g) HAADF-STEM images and (h) EDS elemental maps of HEA intermetallic NPs.

Finally at 700 °C HEA-NPs form with the size ~4.9 nm (**Figure 1h, Figure 3a, and Figure S8**). They possess the fcc structure with random intermixing of all elements, as evidenced by both XRD (**Figure 2e**), STEM imaging and elemental mapping (**Figure 1i and Figure 3b-d**), which is referred to as the HEA solid solution. XPS also unveils the reduction of Pt ions to the near metallic state (**Figure 2f**), indicating the release of most metal atoms at this temperature. Moreover, further raising temperature to 1000 °C induces disorder-to-order transition that transforms the HEA solid solution to $L1_0$ intermetallic, as evidenced by the 100 and 110 diffraction peaks in XRD (**Figure 2e**) that should be extinct for the fcc structure[22]. The *Z*-contrast in the high angle annular dark-field (HAADF) STEM image clearly unveils two sublattices of the $L1_0$ structure, with the bright atomic columns corresponding to pure Pt and the dark columns corresponding to the intermixed TM_{3d} (**Figure 3f-g**), in stark contrast to the solid-solution structure. EDS mapping shows uniform elemental distribution of all TM_{3d} and Pt (**Figure 3h**), confirming their intermixed state. For EXAFS analysis (**Figure S4a**), the peak assigned to Pt-N/O completely disappears and the peak at higher bond length. The same peak is observed on Fe EXAFS, and thus should correspond to Pt-TM_{3d}. The dominance of Pt-TM_{3d} compared to Pt-Pt and TM_{3d}-TM_{3d} bonding (**Figure 2b and 2d**) is consistent with the $L1_0$ structure in which every TM_{3d} atoms are surrounded by eight nearest-neighbor Pt atoms and vice versa, which also distinguish it from the HEA solid solution. The average atomic ratio of Pt/Fe/Co/Ni/Mn is estimated to be 45/18/12/15/10 as confirmed by EDS (**Figure S9**).

Utilizing the surface sensitivity of back scattered electron (BSE) imaging in STEM, a comparison of simultaneously acquired HAADF and BSE images evinces that most nanoparticles are confined within the carbon shells rather than supported on the surface (**Figure S10a-b**). Such carbon confinement helps to stabilize the ultrasmall nanoparticles with an average size of ~5.9 nm without particle aggregation (**Figure S10c**). Even prolonged heating up to 4 hours at 1000 °C causes no obvious particle growth and the intermetallic structure can be well-maintained (**Figure S11**), demonstrating unusual thermal stability especially for such ultrasmall nanoparticles. The detailed carbon-confinement annealing process to form HEA-NPs, as unraveled from the above *ex situ* characterization, is summarized in **Figure 1a**.

To prove the versatility of the carbon-confinement synthesis, we further make binary (PtMn), ternary ($PtFe_{0.5}Mn_{0.5}$, $PtFe_{0.5}Co_{0.5}$), and quaternary ($PtFe_{1/3}Co_{1/3}Mn_{1/3}$, $PtFe_{1/3}Co_{1/3}Ni_{1/3}$) NPs using the same approach (see **Figure S12-16** for details). All NPs after 1000 °C annealing possess the ordered $L1_0$ intermetallic structure with uniform dispersion and without detectable phase separation. We note that HEA intermetallic NPs have so far only been achieved using two-step joule heating, with the first heating to generate HEA alloys and the second to induce disorder-to-order transition[13]. Our carbon-confinement annealing thus represents the first one-step furnace heating to make HEA intermetallic NPs.

It is widely acknowledged that the major challenge to synthesize HEA-NPs is to achieve the proper kinetics that is slow enough to form sufficient crystallinity, but fast enough to avoid thermodynamic-driven phase separation[12]. Then how can carbon confinement prevent phase separation even during the slow furnace annealing? To address this question, we have carried out a control experiment and prepared metal precursors on carbon black support (Vulcan XC-72) without confinement (see **Figure S17** for details). As expected, furnace annealing leads to preferential crystallization of Pt (**Figure S18-19**) at low temperature (300 °C), owing to the lower reduction potential of Pt compared to other TM_{3d}. Further raising temperature leads to considerable phase separation (**Figure S20-21**) and wider size distribution (**Figure S22**). Detailed comparison further unravels the essential role of carbon confinement in making single-phase HEA-NPs, with the following identified merits:

i) It enables the uniform distribution of metal atoms in the single-atom states anchored on the hydroxy and amino groups of dopamine. This is analogous to the catalytic-driven particle dispersion on the surface defect sites as proposed by Yao et al. for their carbothermal shock synthesis[12]. Such uniform dispersion is critical to prevent inhomogeneous nucleation of metals and the resultant phase separation in the following heat treatment.

ii) The disparate reduction potential for various metal precursors can also cause inhomogeneous nucleation, as reflected by the preferential Pt nucleation at 300 °C in the control experiment. Such preferential nucleation has been substantially restrained by carbon confinement, suggesting that the anchoring effect from the hydroxy and amino groups of dopamine can stabilize the dispersed metal ions in such a way that different metals are reduced in a nearly synchronized way to form HEA-NPs without phase separation. This is also conceptually similar to the polymer nanoreactor-mediated synthesis which preconfines precursor in a nanoreactor to form alloyed nanoparticles, avoiding the issues of disparate reduction potentials and elemental-specific nucleation [23] [24].

iii) It inhibits NP growth and agglomeration during high-temperature annealing, offering exceptional high thermal stability. Such volume confinement also helps to prohibit phase separation: with such a small volume, the energy decrease from the thermodynamic-driven phase separation is relatively small, which mitigates the driving force. This is the reason that many metastable structures can be stabilized at the ultrasmall dimension[25]. As for HEA-NPs, a correlation between phase separation and nanoparticle volume increase has been reported[14], both occurring at slow heating/cooling rates[12], which further validates our consideration.

We anticipate that the above three merits of carbon confinement effectively suppress thermodynamic-driven phase separation and enable HEA-NPs synthesis with slow furnace annealing.

Electrochemical oxygen reduction reaction performance

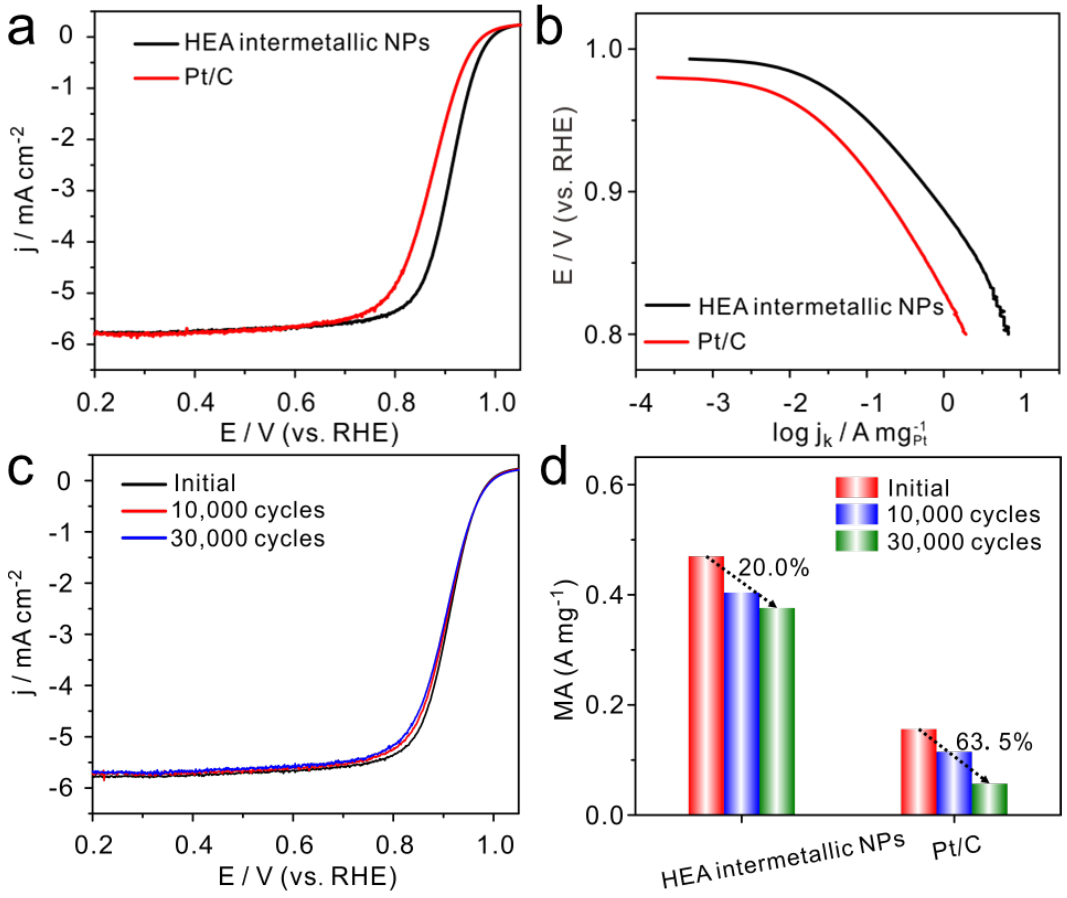

Figure 4. (a) LSV and (b) Tafel curves of both carbon-confined HEA intermetallic NPs and conventional Pt/C. (c) LSV curves of carbon-confined HEA intermetallic NPs at different potential cycles. (d) Comparison of MAs of carbon-confined HEA intermetallic NPs and Pt/C at 0.9 V before and after 10,000 and 30,000 potential cycles.

With a majority of HEA-NPs embedded in the carbon shells, it immediately raises the question whether such carbon confinement may block the surface metal sites and compromise the catalytic performance. We then tested the carbon-confined HEA intermetallic $Pt_{0.45}Fe_{0.18}Co_{0.12}Ni_{0.15}Mn_{0.10}$ in ORR catalysis. Both the linear sweep voltammetry (LSV, **Figure 4a**) and the Tafel plot (**Figure 4b**) show significantly enhanced ORR kinetics of HEA-NPs compared to Pt/C, evidencing sufficient active sites available to catalyze ORR. The special hollow structure of the carbon support should help to maximize the exposed active sites. The electron transfer number is calculated to be ~4 based on Koutecky–Levich plots (**Figure S23**), suggesting the 4e- pathway dominated electrocatalytic ORR[26]. The CO stripping test further reveals the weakened adsorption of oxygen species from the negative shift of CO oxidation peak (**Figure S24**, 0.767 V for HEA-NPs and 0.809 V for Pt/C), reflecting the unique surface active sites from the high-entropy configuration of HEA-NP[22].

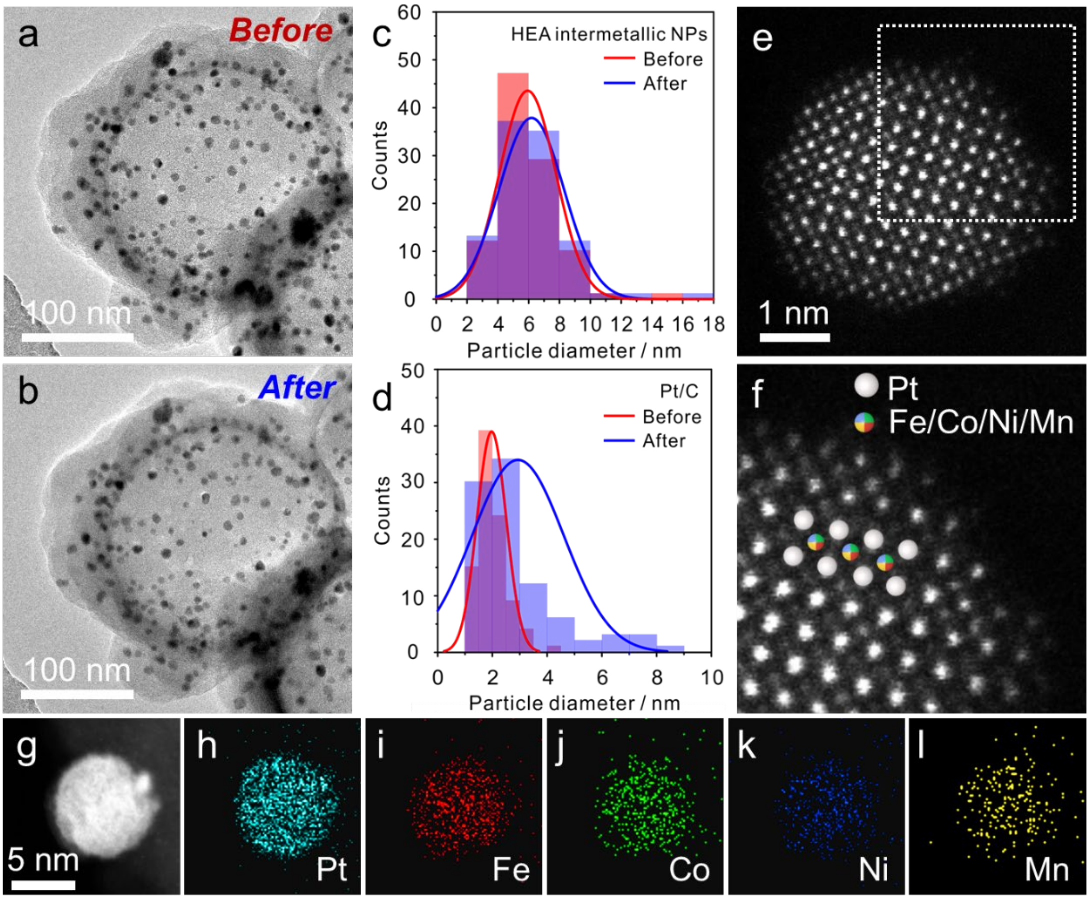

Figure 5. (a,b) Identical-location TEM images and (c) size distribution of HEA intermetallic before and after stability test. (d) Size distribution of Pt/C before and after stability test. (e,f) HAADF-STEM images of a HEA intermetallic NP. (g-l) HAADF-STEM image and corresponding EDS maps of a HEA intermetallic NP after 30,000 potential cycles.

Besides the enhanced activity as can be expected from the high-entropy configuration and ultrasmall size, HEA-NPs also exhibit superior electrochemical stability even in the harsh acid environment of proton exchange membrane fuel cells: After 30,000 cycles, there is nearly no attenuation in the half-wave potential of the LSV curves (**Figure 4c**), and only 20% decrease in the calculated mass activity (MA) at 0.9 V (**Figure 4d**), which is far beyond the 2025 DOE target (<40% loss). CO stripping voltammetry only shows a positive shift of 21 mV after cycling (**Figure S25**), indicating little change on the surface structure. The electrochemical stability of HEA-NPs has been validated explicitly by identical-location TEM (see supporting information for detail), which can track the morphology and structure evolution at the identical place before and after cycling. As shown in **Figure 5a-b**, only slight particles movement can be observed after stability test with negligible particle growth (**Figure 4c**). The $L1_0$ structure is also well maintained (**Figure 5e-f**) after cycling with uniform elemental distribution and no phase separation (**Figure 5g-l and Figure S26**). In contrast, Pt/C experiences serious dissolution-deposition (red cycles) and particle migration (**Figure S27**), with severe particle growth and broadened size distribution (**Figure 5d**)

In summary, a hollow-carbon confinement strategy is developed to achieve HEA-NPs from crystalline solid solution to intermetallic even with the slow furnace annealing. The easy temperature control enables us to unveil the detailed formation process using various *ex situ* characterizations. During this process, the pre-confinement of metal precursor is key to ensure the uniform dispersion of each metal atom. The strong anchoring effect also helps release different atoms slowly, benefiting the formation of small nuclei that grow into HEA-NPs. Together with carbon confinement, particle growth and aggregation can be inhibited, greatly avoiding the unwanted thermodynamic-driven phase separation process. The resultant hollow-carbon support further ensures sufficient exposed surface, giving rise to superior ORR performance in terms of both activity and stability. Overall, our hollow-carbon confinement furnace annealing provides an alternative synthetic approach that is expected to be broadly applicable, promising for further expanding the scope of achievable HEA-NPs for various applications.

Supporting information

The Supporting Information is available free of charge on the ACS Publications website at DOI:

Material preparation, physical characterizations (XPS, XRD, XAS, TEM), electrochemical measurement (K-L, CO stripping). (PDF).

Author information

Corresponding Authors

*E-mail: yezhu@polyu.edu.hk

Acknowledgements

This work was financially supported by the Research Grants Council of Hong Kong (project no. C5029-18E) and the Hong Kong Polytechnic University grant (no. ZVRP)

References

(1) Mori, K.; Hashimoto, N.; Kamiuchi, N.; Yoshida, H.; Kobayashi, H.; Yamashita, H.

Hydrogen spillover-driven synthesis of high-entropy alloy nanoparticles as a robust catalyst for CO_2 hydrogenation. *Nat. Commun.* **2021**, *12* (1), 3884. DOI: https://doi.org/10.1038/s41467-021-24228-z.

(2) Xin, Y.; Li, S.; Qian, Y.; Zhu, W.; Yuan, H.; Jiang, P.; Guo, R.; Wang, L. High-Entropy Alloys as a Platform for Catalysis: Progress, Challenges, and Opportunities. *ACS Catal.* **2020**, *10* (19), 11280-11306. DOI: https://doi.org/10.1021/acscatal.0c03617.

(3) Li, H.; Lai, J.; Li, Z.; Wang, L. Multi-Sites Electrocatalysis in High-Entropy Alloys. *Adv. Funct. Mater.* **2021**, *31* (47), 2106715. DOI: https://doi.org/10.1002/adfm.202106715.

(4) Tao, L.; Sun, M.; Zhou, Y.; Luo, M.; Lv, F.; Li, M.; Zhang, Q.; Gu, L.; Huang, B.; Guo, S. A General Synthetic Method for High-Entropy Alloy Subnanometer Ribbons. *J. Am. Chem. Soc.* **2022**, *144* (23), 10582-10590. DOI: https://doi.org/10.1021/jacs.2c03544.

(5) Zhu, G.; Jiang, Y.; Yang, H.; Wang, H.; Fang, Y.; Wang, L.; Xie, M.; Qiu, P.; Luo, W. Constructing Structurally Ordered High-Entropy Alloy Nanoparticles on Nitrogen-Rich Mesoporous Carbon Nanosheets for High-Performance Oxygen Reduction. *Adv. Mater.* **2022**, *34* (15), 2110128. DOI: https://doi.org/10.1002/adma.202110128.

(6) Fu, X.; Zhang, J.; Zhan, S.; Xia, F.; Wang, C.; Ma, D.; Yue, Q.; Wu, J.; Kang, Y. High-Entropy Alloy Nanosheets for Fine-Tuning Hydrogen Evolution. *ACS Catal.* **2022**, *12* (19), 11955-11959. DOI: https://doi.org/10.1021/acscatal.2c02778.

(7) Luo, H.; Wang, K.; Lin, F.; Lv, F.; Zhou, J.; Zhang, W.; Wang, D.; Zhang, W.; Zhang, Q.; Gu, L.; Luo, M.; Guo, S. Amorphous MoOx with high oxophilicity interfaced with

PtMo alloy nanoparticles boosts anti-CO hydrogen electrocatalysis. *Adv. Mater.* **2023**, 2211854. DOI: https://doi.org/10.1002/adma.202211854.

(8) Wu, S.; Pan, Y.; Lu, J.; Wang, N.; Dai, W.; Lu, T. Effect of the addition of Mg, Ti, Ni on the decoloration performance of AlCrFeMn high entropy alloy. *J. Mater. Sci. Technol.* **2019**, *35* (8), 1629-1635. DOI: https://doi.org/10.1016/j.jmst.2019.03.025.

(9) Motallebzadeh, A.; Peighambardoust, N. S.; Sheikh, S.; Murakami, H.; Guo, S.; Canadinc, D. Microstructural, mechanical and electrochemical characterization of TiZrTaHfNb and $Ti_{1.5}ZrTa_{0.5}Hf_{0.5}Nb_{0.5}$ refractory high-entropy alloys for biomedical applications. *Intermetallics* **2019**, *113*, 106572. DOI: https://doi.org/10.1016/j.intermet.2019.106572.

(10) Batchelor, T. A. A.; Pedersen, J. K.; Winther, S. H.; Castelli, I. E.; Jacobsen, K. W.; Rossmeisl, J. High-Entropy Alloys as a Discovery Platform for Electrocatalysis. *Joule* **2019**, *3* (3), 834-845. DOI: https://doi.org/10.1016/j.joule.2018.12.015.

(11) Yao, Y.; Dong, Q.; Brozena, A.; Luo, J.; Miao, J.; Chi, M.; Wang, C.; Kevrekidis, I. G.; Ren, Z. J.; Greeley, J.; Wang, G.; Anapolsky, A.; Hu, L. High-entropy nanoparticles: Synthesis-structure-property relationships and data-driven discovery. *Science* **2022**, *376* (6589), eabn3103. DOI: https://doi.org/doi:10.1126/science.abn3103.

(12) Yao, Y.; Huang, Z.; Xie, P.; Lacey, S. D.; Jacob, R. J.; Xie, H.; Chen, F.; Nie, A.; Pu, T.; Rehwoldt, M.; Yu, D.; Zachariah, M. R.; Wang, C.; Shahbazian-Yassar, R.; Li, J.; Hu, L. Carbothermal shock synthesis of high-entropy-alloy nanoparticles. *Science* **2018**, *359* (6383), 1489-1494. DOI: https://doi.org/10.1126/science.aan5412.

(13) Xie, P.; Yao, Y.; Huang, Z.; Liu, Z.; Zhang, J.; Li, T.; Wang, G.; Shahbazian-Yassar, R.; Hu, L.; Wang, C. Highly efficient decomposition of ammonia using high-entropy alloy catalysts. *Nat. Commun.* **2019**, *10* (1), 4011. DOI: https://doi.org/10.1038/s41467-019-11848-9.

(14) Cui, M.; Yang, C.; Hwang, S.; Yang, M.; Overa, S.; Dong, Q.; Yao, Y.; Brozena, A. H.; Cullen, D. A.; Chi, M.; Blum, T. F.; Morris, D.; Finfrock, Z.; Wang, X.; Zhang, P.; Goncharov, V. G.; Guo, X.; Luo, J.; Mo, Y.; Jiao, F.; Hu, L. Multi-principal elemental intermetallic nanoparticles synthesized via a disorder-to-order transition. *Sci. Adv.* **2022**, *8* (4), eabm4322. DOI: https://doi.org/doi:10.1126/sciadv.abm4322.

(15) Li, T.; Yao, Y.; Huang, Z.; Xie, P.; Liu, Z.; Yang, M.; Gao, J.; Zeng, K.; Brozena, A. H.; Pastel, G.; Jiao, M.; Dong, Q.; Dai, J.; Li, S.; Zong, H.; Chi, M.; Luo, J.; Mo, Y.; Wang, G.; Wang, C.; Shahbazian-Yassar, R.; Hu, L. Denary oxide nanoparticles as highly stable catalysts for methane combustion. *Nat. Catal.* **2021**, *4* (1), 62-70. DOI: https://doi.org/10.1038/s41929-020-00554-1.

(16) Zuo, X.; Yan, R.; Zhao, L.; Long, Y.; Shi, L.; Cheng, Q.; Liu, D.; Hu, C. A hollow PdCuMoNiCo high-entropy alloy as an efficient bi-functional electrocatalyst for oxygen reduction and formic acid oxidation. *J. Mater. Chem. A* **2022**, *10* (28), 14857-14865, 10.1039/D2TA02597C. DOI: https://doi.org/10.1039/D2TA02597C.

(17) Bondesgaard, M.; Broge, N. L. N.; Mamakhel, A.; Bremholm, M.; Iversen, B. B. General Solvothermal Synthesis Method for Complete Solubility Range Bimetallic and High-Entropy Alloy Nanocatalysts. *Adv. Funct. Mater.* **2019**, *29* (50), 1905933. DOI: https://doi.org/10.1002/adfm.201905933.

(18) Chen, W.; Luo, S.; Sun, M.; Wu, X.; Zhou, Y.; Liao, Y.; Tang, M.; Fan, X.; Huang, B.; Quan, Z. High-Entropy Intermetallic PtRhBiSnSb Nanoplates for Highly Efficient Alcohol Oxidation Electrocatalysis. *Adv. Mater.* **2022**, *34* (43), 2206276. DOI: https://doi.org/10.1002/adma.202206276.

(19) Chen, Y.; Zhan, X.; Bueno, S. L. A.; Shafei, I. H.; Ashberry, H. M.; Chatterjee, K.; Xu, L.; Tang, Y.; Skrabalak, S. E. Synthesis of monodisperse high entropy alloy nanocatalysts from core@shell nanoparticles. *Nanoscale Horiz.* **2021**, *6* (3), 231-237, DOI: https://doi.org/10.1039/D0NH00656D.

(20) Bueno, S. L. A.; Leonardi, A.; Kar, N.; Chatterjee, K.; Zhan, X.; Chen, C.; Wang, Z.; Engel, M.; Fung, V.; Skrabalak, S. E. Quinary, Senary, and Septenary High Entropy Alloy Nanoparticle Catalysts from Core@Shell Nanoparticles and the Significance of Intraparticle Heterogeneity. *ACS Nano* **2022**, *16* (11), 18873-18885. DOI: https://doi.org/10.1021/acsnano.2c07787.

(21) Wang, Z.; Zou, Y.; Li, Y.; Cheng, Y. Metal-Containing Polydopamine Nanomaterials: Catalysis, Energy, and Theranostics. *Small* **2020**, *16* (18), 1907042. DOI: https://doi.org/10.1002/smll.201907042.

(22) Hu, Y.; Guo, X.; Shen, T.; Zhu, Y.; Wang, D. Hollow Porous Carbon-Confined Atomically Ordered $PtCo_3$ Intermetallics for an Efficient Oxygen Reduction Reaction. *ACS Catal.* **2022**, *12* (9), 5380-5387. DOI: https://doi.org/10.1021/acscatal.2c01541.

(23) Chen, P.-C.; Liu, X.; Hedrick, J. L.; Xie, Z.; Wang, S.; Lin, Q.-Y.; Hersam, M. C.; Dravid, V. P.; Mirkin, C. A. Polyelemental nanoparticle libraries. *Science* **2016**, *352* (6293), 1565-1569. DOI: https://doi.org/10.1126/science.aaf8402.

(24) Chen, P.-C.; Liu, M.; Du, J. S.; Meckes, B.; Wang, S.; Lin, H.; Dravid, V. P.; Wolverton, C.; Mirkin, C. A. Interface and heterostructure design in polyelemental nanoparticles. *Science* **2019**, *363* (6430), 959-964. DOI: https://doi.org/10.1126/science.aav4302.

(25) Curtarolo, S.; Setyawan, W.; Wang, S.; Xue, J.; Yang, K.; Taylor, R. H.; Nelson, L. J.; Hart, G. L. W.; Sanvito, S.; Buongiorno-Nardelli, M.; Mingo, N.; Levy, O. AFLOWLIB.ORG: A distributed materials properties repository from high-throughput ab initio calculations. *Comput. Mater. Sci.* **2012**, *58*, 227-235. DOI: https://doi.org/10.1016/j.commatsci.2012.02.002.

(26) Hu, Y.; Lu, Y.; Zhao, X.; Shen, T.; Zhao, T.; Gong, M.; Chen, K.; Lai, C.; Zhang, J.; Xin, H. L.; Wang, D. Highly active N-doped carbon encapsulated Pd-Fe intermetallic nanoparticles for the oxygen reduction reaction. *Nano Res.* **2020**, *13*, 2365-2370. DOI: https://doi.org/10.1007/s12274-020-2856-z.

For Table of Contents Only